Magnetic Nanoparticles

DOI: 10.1002/anie.200701674

Chemical Design of Nanoparticle Probes for High-Performance Magnetic Resonance Imaging

*Young-wook Jun, Jae-Hyun Lee, and Jinwoo Cheon**

Keywords:
magnetic properties · magnetic resonance imaging · medicinal chemistry · nanoparticles · nanotechnology

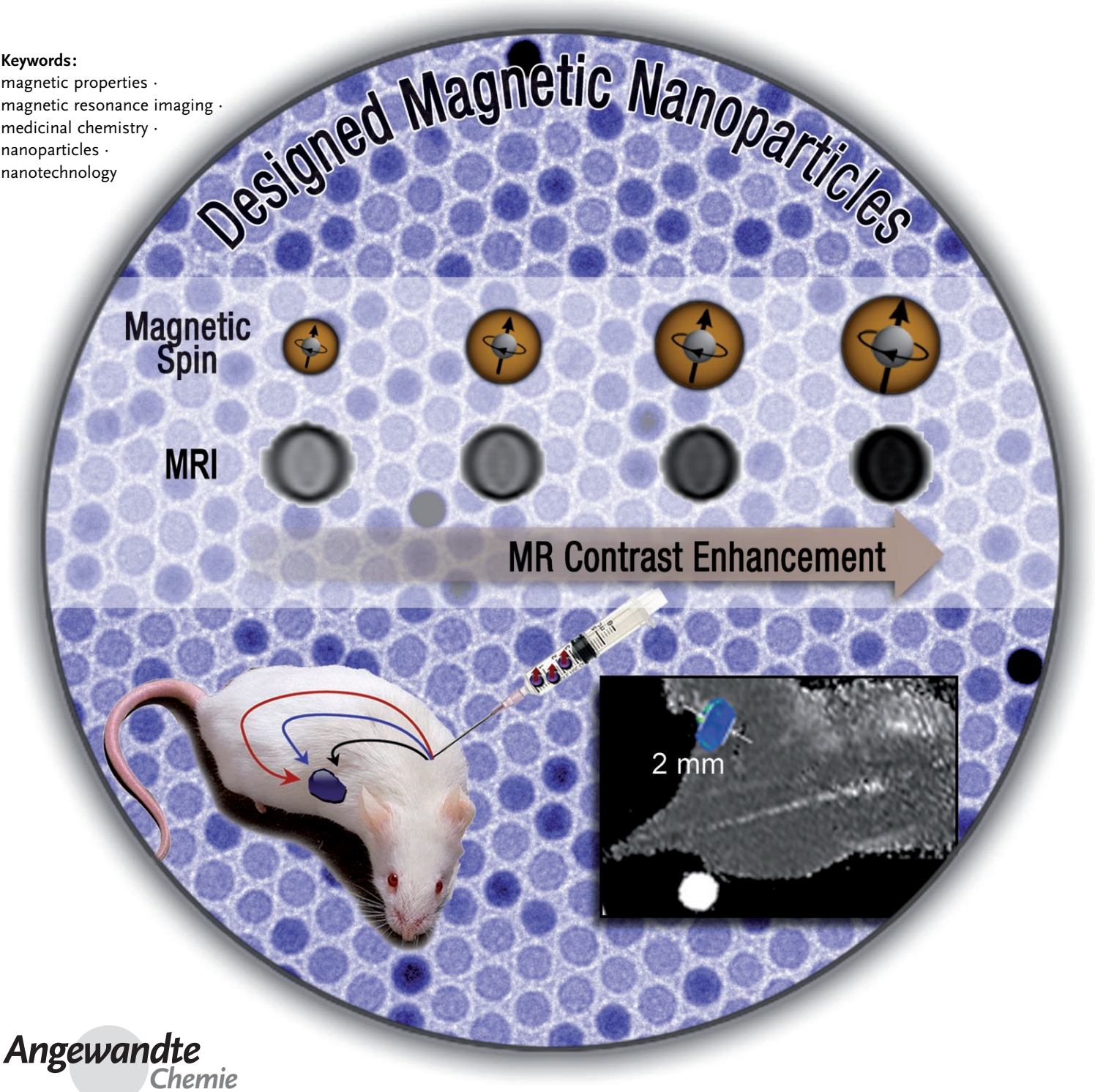

© 2008 Wiley-VCH Verlag GmbH & Co. KGaA, Weinheim

Synthetic magnetic nanoparticles (MNPs) are emerging as versatile probes in biomedical applications, especially in the area of magnetic resonance imaging (MRI). Their size, which is comparable to biological functional units, and their unique magnetic properties allow their utilization as molecular imaging probes. Herein, we present an overview of recent breakthroughs in the development of new synthetic MNP probes with which the sensitive and target-specific observation of biological events at the molecular and cellular levels is possible.

From the Contents

1. Introduction

The development of biomedical imaging techniques, such as computed X-ray tomography (CT), optical imaging, and magnetic resonance imaging (MRI), has brought significant advances for diagnosis and therapy.[1–3] Since most biological processes and diseases occur at the molecular and cellular levels, however, the precise real-time imaging and the understanding of these processes are still challenging.

Inorganic nanoparticles are emerging as promising probes with which to shed light on these unexplored events. They have the potential for advancing imaging from its current anatomy-based level to the molecular level, so-called "molecular imaging".[4–9] Upon conjugation with target-specific biomolecules, these tiny probes (1–100 nm) can travel through the human body in the blood and lymphatic vessels[10,11] and they can identify the desired target by specific biological interactions, such as antibody–antigen,[4,6,7,12,13] nucleic acid hybridization,[14–18] and gene expression.[19–21]

For the past two decades, nature-inspired or aqueous-phase synthetic iron oxide nanoparticles, such as dextran-coated superparamagnetic iron oxide (SPIO) and related nanoparticles (e.g. cross-linked iron oxide (CLIO), Feridex, Resovist, and Combidex) have served as contrast-enhancing probes for MRI (see Table 1).[7,8] Some forms of these nanoparticles are now clinically used for improving anatomical magnetic resonance (MR) contrast[22,23] and have also been used in molecular imaging.[21,24] To improve MR contrast effects and incorporate more versatile surface groups for advanced molecular imaging, researchers have been developing next-generation MNP probes. Fortunately, rapid advances in non-hydrolytic thermal-decomposition synthetic methods for preparing MNPs have allowed researchers to synthetically control the important features of these probes, such as size, magnetic dopants, magneto-crystalline phases, and surface states,[25–36] resulting in the discovery of "designed" MNPs. These innovative nanoparticle probes exhibit superior magnetism and MR contrast effects which have been shown to be better than that of conventional MNP MR contrast agents.[37–42] Herein, we will provide an overview of the strategies for the design of such new types of MNP. Specifically, we focus on the two most representative types of iron oxide based MNPs and metal alloy MNPs. In addition we consider the following points: 1) MR contrast enhancement by control of the magnetic core (Figure 1 a), 2) design of

Table 1: Conventional and new types of nanoparticle-based MRI contrast agents.

Name	Magnetic core size [nm]	Total size [nm]	Coating material	$r2$[a] [$mM^{-1}s^{-1}$]	B [T]
		Conventional MNP Agents			
AMI-25 (Feridex; Endorem)[51]	5–6	80–150	Dextran	ca. 100	0.47
SHU 555A (Resovist)[52]	ca. 4.2	ca. 62	Carbodextran	151	0.47
AMI-227 (Combidex; Sinerem)[53]	4–6	20–40	Dextran	53	0.47
CLIO; MION[54]	ca. 2.8	10–30	Dextran	ca. 69	1.5
		New Types of Synthetic MNPs			
Fe_3O_4 (MEIO)[38]	12	15	DMSA	218	1.5
$MnFe_2O_4$ (MnMEIO)[38]	12	15	DMSA	358	1.5
FeCo[39]	7	30	Carbon and phospholipids-poly(ethylene glycol)	644	1.5

[a] The $r2$ values are literature values and can be slightly variable depending on the field strength and MR pulse sequences.

[*] Dr. Y.-w. Jun, J.-H. Lee, Prof. J. Cheon
Department of Chemistry
Yonsei University
Seoul 120-749 (Korea)
Fax: (+82) 2-364-7050
E-mail: jcheon@yonsei.ac.kr

© 2008 Wiley-VCH Verlag GmbH & Co. KGaA, Weinheim

the ligand shell to attain high colloidal stability and biocompatibility (Figure 1b), 3) molecular and cellular targeting capabilities (Figure 1c), and 4) MR imaging of cancer, angiogenesis, cell trafficking, and therapy (Figure 1d).

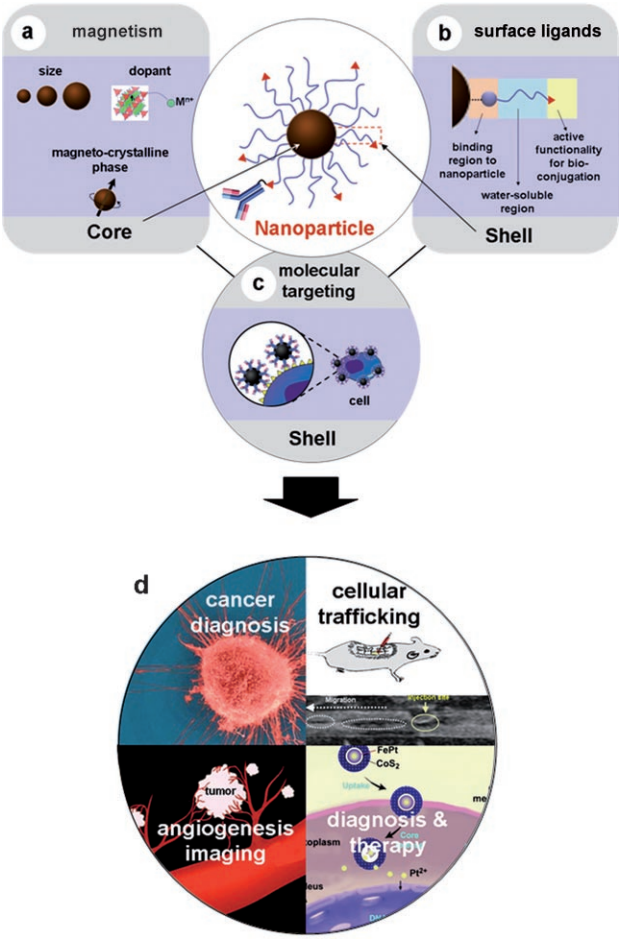

Figure 1. Tailored MNPs for molecular and cellular magnetic resonance imaging (MRI). a) Controlling the magnetism of the nanoparticle core, b) tailoring the surface ligands of the nanoparticle shell, and c) the molecular targeting capability of biomolecule-conjugated nanoparticles. d) High performance utilizations of nanoparticles for molecular and cellular MRI.

2. Synthesis of High-Performance MNP Probes

2.1. MR Contrast-Enhancement Strategies

2.1.1. Basic Principles of MR Contrast Enhancement

Under an applied magnetic field (B_0), a magnetic dipole moment μ is induced in superparamagnetic nanoparticles. When water molecules diffuse into the periphery (outer sphere) of the induced dipole moment, the magnetic relaxation processes of the water protons are perturbed and the spin–spin relaxation time ($T2$) is shortened. Such changes result in the darkening of the corresponding area in $T2$-weighted MR images (Figure 2). The degree of the $T2$ contrast effect is typically represented by the spin–spin relaxivity $R2$ ($R2 = 1/T2$), where higher values of $R2$ result in a greater contrast effect. The relaxivity coefficient ($r2$), which is obtained as the gradient of the plot of $R2$ versus the molarity of magnetic atoms, is a standardized contrast-enhancement indicator.

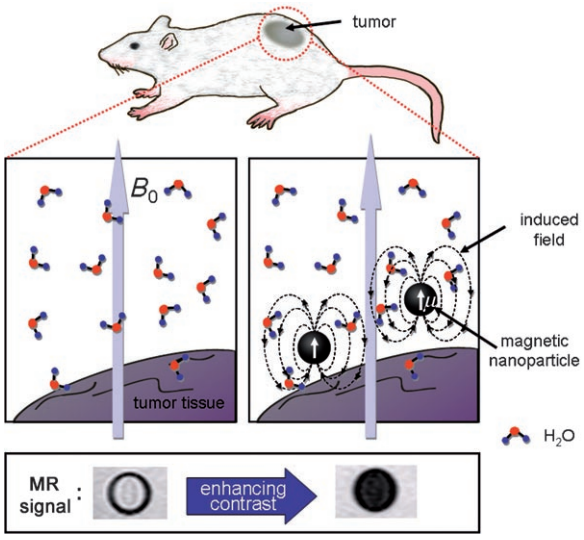

Figure 2. MR contrast effects of MNPs. Under an external field (B_0), MNPs are magnetized with a magnetic moment of μ and generate an induced magnetic field which perturbs the nuclear spin relaxation processes of the water protons. This perturbation leads to MR contrast enhancement which appears as a darkening of the corresponding section of the image.

Jinwoo Cheon graduated from Yonsei University and received his Ph.D. from University of Illinois, Urbana-Champaign in 1993. After post-doctoral training at U.C. Berkeley and also at UCLA, he joined the KAIST where he was an assistant and then associate professor. In 2002, he returned to Yonsei University. He is the director of the Convergence Nanomaterials National Research Laboratory and the head of the Nanomaterials Division of the Nano-Medical National Core Research Center of Korea. His research interests include the development of functional inorganic nanoparticles and their biomedical and energy related applications.

Young-wook Jun studied at Yonsei University and received his Ph.D. degree from the Korea Advanced Institute of Science and Technology (KAIST; 2005), where he studied the synthetic and mechanistic aspects of inorganic nanocrystals under the guidance of Professors Sang Youl Kim and Jinwoo Cheon. He then studied the magnetic nanoparticles for biological targets at Yonsei University. Currently he is carrying out postdoctoral studies with Professor Paul Alivisatos on nanoparticle assisted single-molecule spectroscopy at the U.C. Berkeley. He is a recipient of the Honorable Mention Award of the IUPAC Prize for Young Chemists (2005).

© 2008 Wiley-VCH Verlag GmbH & Co. KGaA, Weinheim

Based on this outer-sphere relaxation model with solute magnetic nanoparticles, the $R2$ of the proton can be determined by Equation (1).[43]

$$R2 = \frac{1}{T2} = \left(\frac{32\pi}{405}\right)\gamma_I^2\mu^2\frac{N_A}{1000}\left(\frac{[M]}{rD}\right)\{6.5\,j_2(\omega_S) + 1.5\,j_1(\omega_I) + 2\,j_1(0)\}$$

$$j_n(\omega,\tau,\tau_{Sn}) = Re\left(\frac{1 + {}^1/_4(i\omega\tau + \tau/\tau_{Sn})^{1/2}}{1 + (i\omega\tau + \tau/\tau_{Sn})^{1/2} + {}^4/_9(i\omega\tau + \tau/\tau_{Sn}) + {}^1/_9(i\omega\tau + \tau/\tau_{Sn})^{3/2}}\right)^2 \quad (1)$$

Where, γ_I is the gyromagnetic ratio of protons in water, M is the molarity of the magnetic nanoparticle, r is its radius, N_A is Avogadro's number, μ is the magnetic moment of the nanoparticle, ω_S and ω_I are the Larmor angular precession frequencies of the nanoparticle electric moment and water proton magnetic moment, respectively, the functions $j_n(\omega, \tau)$ are spectral density functions in which Re is the real part of the expression that follows in parenthesis, τ ($\tau = r^2/D$) is the time scale of fluctuations in the particle–water proton magnetic dipolar interaction arising from the relative diffusive motion (D) of a particle with respect to water molecules, and τ_{S1} and τ_{S2} are the lifetimes of the longitudinal and transverse components of μ.[43]

The control of nanoparticle magnetism should be conducted so as to lead to a maximum value of $R2$. Since $R2$ is strongly related to the magnetic moment (μ) and the relaxation processes of the magnetic spin (τ_{S1}, τ_{S2}), maximization of μ during nanoparticle synthesis is important. The magnetic moment (μ) of the nanoparticle is dependent on the size, composition, and magneto-crystalline phase of the nanoparticle. The lifetimes of the longitudinal and transverse components of μ correlate with the magneto-crystalline phase of the nanoparticles. Therefore, by precisely modulating these nanoparticle parameters, synthetic MNPs can be designed and constructed to maximize the MR contrast-enhancement effects (Figure 3).

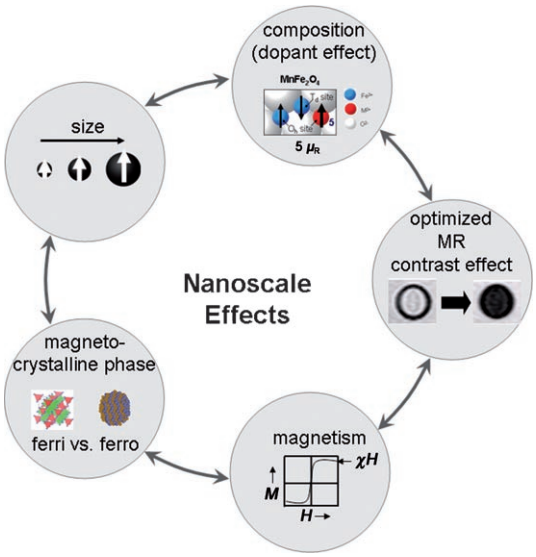

Figure 3. Important parameters of MNPs for MR contrast-enhancement effects.

2.1.2. *Synthesis of MNPs*

High-quality synthetic MNPs are typically prepared through the thermal decomposition of metal-complex precursors in hot non-hydrolytic organic solution containing surfactants. Thermal decomposition of the precursors generates monomers and their aggregation above a supersaturation level induces nucleation and subsequent nanoparticle growth.[44–48] During these stages, by tuning growth parameters, such as monomer concentration, crystalline phase of the nuclei, choice of solvent and surfactants, growth temperature and time, and surface energy, it is possible to control the size, composition, and magneto-crystalline phase of MNPs. For example, there have been many reports on the synthesis of metal ferrite nanoparticles from precursors such as iron pentacarbonyl, iron cupferron, iron tris(2,4-pentadionate), and iron fatty acid complexes, in hot organic solvents containing fatty acids and amine surfactants.[25,26,28,29,31] Nanoparticle size can be tuned within the range of 4 nm to approximately 50 nm with 1–3 nm resolution. Details on the synthesis of such MNPs have been reviewed previously.[32,35,44]

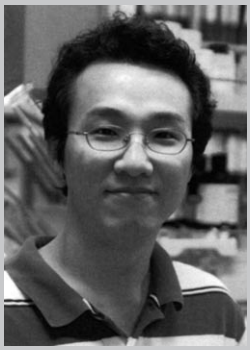

Jae-Hyun Lee, graduated from Yonsei University in 2003 with his B.S. degree. He is currently pursuing his Ph.D. under the supervision of Professor Jinwoo Cheon. His current research interests are the fabrication of bioactivatable hybrid magnetic nanoparticles for molecular imaging and therapeutics. He is a recipient of a Korea Research Foundation Fellowship (2004) and a Seoul Science Fellowship (2005).

2.1.3. *Size Effects of MNPs*

One important parameter for the MR contrast-enhancement effect of MNPs is their size. In the ideal case, all of the magnetic spins in a bulk magnetic material are aligned parallel to the external magnetic field. However, in the nanoscale regime, surface spins tend to be slightly tilted to form a magnetically disordered spin-glass-like surface layer (Figure 4a).[49] Such surface spin-canting effects of MNPs have a significant influence on their magnetic moments and MR contrast-enhancement effects as predicted in Equation (1). This effect is size dependent and is well demonstrated in the case of magnetism-engineered iron oxide (MEIO, Fe_3O_4) nanoparticles, where the variation of their size from 4 nm to 6 nm, 9 mm, and 12 nm results in mass-magnetization values of 25, 43, 80, and 101 emu per gram Fe, respectively (Figure 4b,c).[37] As the nanoparticle size decreases, the surface effect becomes more pronounced and is reflected in the reduced net magnetic moment. Such size-dependent magnetism directly influences the MR enhancement effect. The relaxivity coefficient ($r2$) gradually increases from approximately 78 to 106, 130, and to 218 $mM^{-1}s^{-1}$ for

 © 2008 Wiley-VCH Verlag GmbH & Co. KGaA, Weinheim

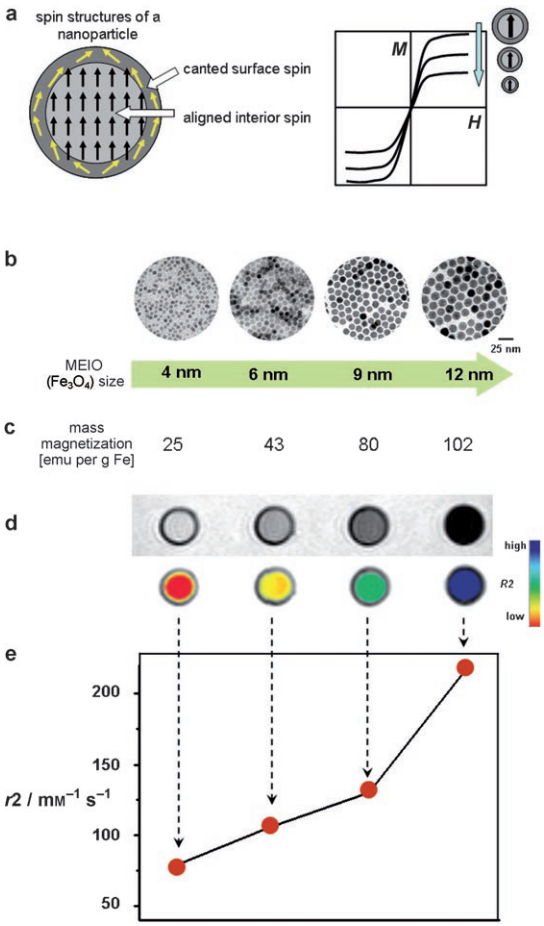

Figure 4. a) Surface spin canting effect of a nanoparticle upon magnetization (*M* magnetic moment, *H* external magnetic field). b–e) Nanoscale size effects of Fe_3O_4 (MEIO) nanoparticles on magnetism and MR contrast effects. b) Transmission electron microscopic (TEM) images of 4, 6, 9, and 12 nm sized MEIO nanoparticles. c) Mass magnetization values, d) *T*2-weighted MR images (top: black and white, bottom: color), and e) relaxivity coefficient *r*2 of the nanoparticles presented in (a); (from Ref. [37]).

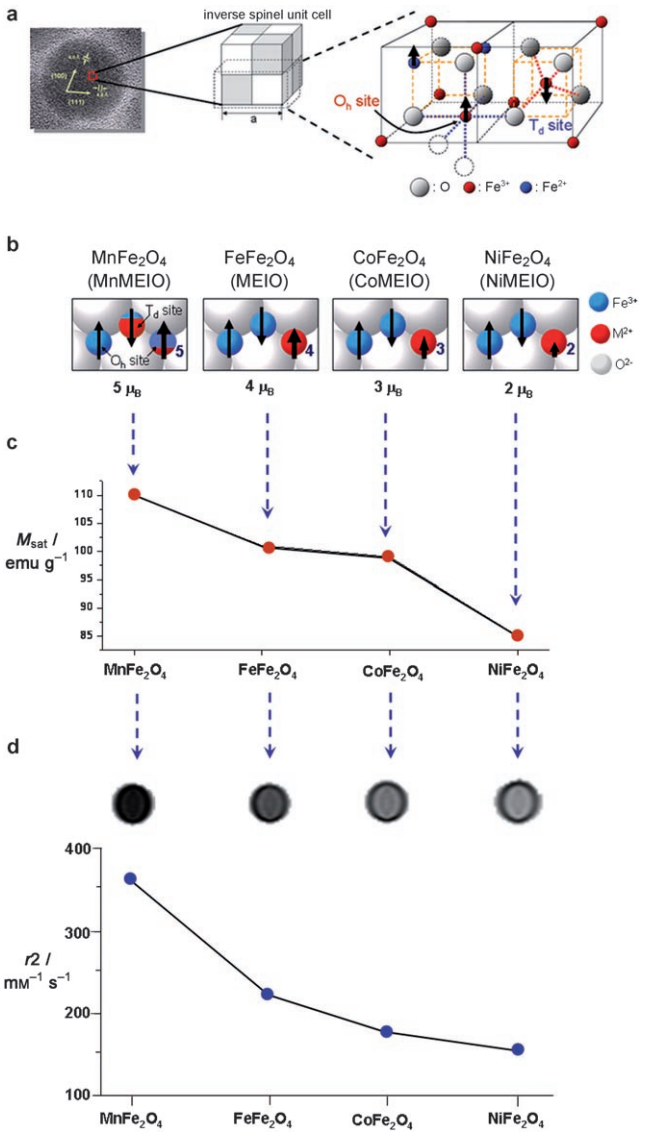

Figure 5. a) Metal ferrite nanoparticle with inverse spinel structure and its ferrimagnetic spin alignments; O_h octahedral hole, T_d tetrahedral hole. b) Magnetic spin structures of metal-doped MEIO nanoparticles, MFe_2O_4 (M = Mn, Fe, Co, Ni) nanoparticles. c) Their dopant-dependent mass magnetization values, and d) effects on MR contrast and the *r*2 (from Ref. [38]).

4 nm, 6 nm, 9 nm, and 12 nm sized nanoparticles, respectively, which is shown by the MR contrast changing from light gray to black (or from red to blue in color-coded images; (Figure 4 d,e).

2.1.4. *Magnetic-Dopant Effects in MNPs*

The magnetism of nanoparticles can be greatly influenced by doping with magnetically susceptible elements. This is demonstrated for MFe_2O_4 nanoparticles in which Fe^{2+} ions are replaced by other transition-metal dopants M^{2+} where M = Mn, Ni, Co.[38] Ferrimagnetic Fe_3O_4 has a crystallographically inverse spinel structure constructed of face-centered cubic packed lattice of oxygen atoms with the tetrahedral sites (T_d) occupied by Fe^{3+} ions and octahedral sites (O_h) occupied by Fe^{3+} and Fe^{2+} ions. Under an external magnetic field, the magnetic spins of the ions at the O_h sites align parallel to the external magnetic field but those at T_d sites align antiparallel to the field (Figure 5 a). Since Fe^{3+} has a d^5 configuration and Fe^{2+} has a d^6 configuration with a high spin state, the total magnetic moment per unit $(Fe^{3+})_{T_d}(Fe^{2+}Fe^{3+})_{O_h}O_4$ is 4 μ_B.[50]

As a result of their electron spin configurations, the magnetic moments per unit $MnFe_2O_4$, $CoFe_2O_4$, and $NiFe_2O_4$ can be estimated as 5 μ_B, 3 μ_B, and 2 μ_B, respectively (Figure 5 b).[50] Mass magnetization measurements clearly reflect the magnetic-dopant effect, the mass magnetization value is highest for $MnFe_2O_4$ nanoparticles (110 emu per gram Mn,Fe) and gradually decreases for $FeFe_2O_4$ (101 emu per gram Fe), $CoFe_2O_4$ (99 emu per gram Co,Fe), and $NiFe_2O_4$ (85 emu per gram Ni,Fe; Figure 5 c).[38]

These metal-doped MEIO nanoparticles can induce significant MR contrast-enhancement effects.[38] Under *T*2-weighted MR scans, $MnFe_2O_4$ (MnMEIO) shows the stron-

 © 2008 Wiley-VCH Verlag GmbH & Co. KGaA, Weinheim

gest MR contrast effect, with an coefficient $r2$ of 358 $mM^{-1}s^{-1}$. The $r2$ values are 218, 172, and 152 $mM^{-1}s^{-1}$, for $FeFe_2O_4$ (MEIO), $CoFe_2O_4$ (CoMEIO), and $NiFe_2O_4$ (NiMEIO) respectively (Figure 5d). The $r2$ of MnMEIO is more than two-times higher than the values of conventional SPIO related MR contrast agents (Table 1). This increased MR contrast-enhancement capability of MNPs is advantageous for example for MR imaging small cancers (see Section 3).

2.1.5. Metal-Alloy MNPs

Metal alloys MNPs, such as FeCo and FePt are another example of MR probes.[32,33,35,55] In these MNPs all the magnetic spins align parallel to the external magnetic field, as a result they typically have higher magnetic moments than those of ferrimagnetic nanoparticles. For example, the magnetic moment of FeCo magnetic alloys is approximately 2.4 μ_B per magnetic atom, while that of Fe_3O_4 is approximately 1.3 μ_B per magnetic atom.[56] Therefore, metal-alloy MNPs can be excellent candidates for MR probes. One successful demonstration has been the development of 7 nm sized FeCo MNPs passivated with a graphite shell (Figure 6a).[39] Coating of the MNPs with phospholipid–poly(ethylene glycol) (PL-PEG) endows them with colloidal stability in aqueous media (Figure 6b). These FeCo MNPs have an exceptionally high magnetization value of 215 emu per gram metal (Figure 6c). The coefficient $r2$ of FeCo MNPs has been determined to be 644 $mM^{-1}s^{-1}$, which is much larger than that of conventional SPIO contrast agents, such as Feridex (ca. 100 $mM^{-1}s^{-1}$).[39] These MNPs are successfully utilized for in vitro cell labeling and in vivo $T1$-weighted blood pool MR imaging (see Section 3 and references [57,58] for reviews on $T1$ agents).

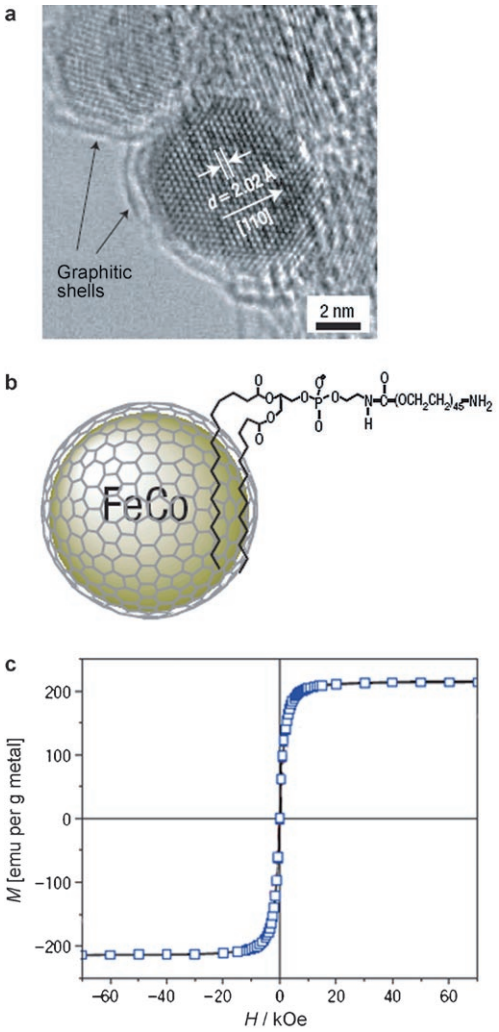

Figure 6. FeCo magnetism-controlled metal-alloy MNPs. a) TEM image. b) Schematic representation of its surface ligand coating. c) Hysteresis loop of 7 nm FeCo nanoparticles (from Ref. [39]).

2.2. Surface Ligands for High Colloidal Stability and Biocompatibility

Nonhydrolytically synthesized MNPs are typically coated with hydrophobic ligands. Therefore it is necessary to exchange these ligands for appropriate ones that will give high colloidal stability in aqueous biofluids and to avoid aggregation which can occur under harsh physiological conditions. The nanoparticle hydrodynamic diameter which is defined as the apparent size of a dynamic hydrated/solvated particle, is highly related to their capabilities for effectively overcoming the biological defense system and vascular barriers. For example, MNPs with a large hydrodynamic diameter (e.g. >100 nm) are readily taken up by phagocytes,[59] but smaller MNPs (e.g. 1–30 nm) can escape from phagocytes and travel through blood vessels with a reasonably high blood half-life (>1 h) (Figure 7a).[60] These relatively small-sized MNPs can have enhanced permeability and retention (EPR) effects at the target tissues because they can easily pass through the larger fenestrations (100 nm to several μm) of the blood vessels in the vicinity of cancerous tissues (Figure 7a).[61,62] Recently, a variety of ligand-exchange strategies for MNPs have been developed (Figure 7b). Since surface engineering and the attachment of biomolecules can change the size of the nanoparticles, more comprehensive studies on nanoparticle size are needed to determine the optimum size that would allow for large $R2$ values with a longer blood half-life.

2.2.1. Bifunctional Ligand Coatings[42,63–69]

Initial attempts to transfer the nanoparticles from organic to aqueous media were performed by introducing small bifunctional molecules as ligands.[63–65] The ligand is typically composed of two parts—the region which binds to the MNP surface and the hydrophilic region that will be exposed to the aqueous medium. For example, the diol moiety of betaine molecules attach to the iron oxide nanoparticles and the ammonium salt at the opposite end makes them water soluble.[64]

The use of the PEG moiety as a hydrophilic group can enhance colloidal stability of nanoparticles.[66–69] For example, introducing mixed bifunctional ligands, such as PEG–thiol and PEG–dopamine onto FePt[66] or Fe@Fe_3O_4[66] nanopar-

© 2008 Wiley-VCH Verlag GmbH & Co. KGaA, Weinheim

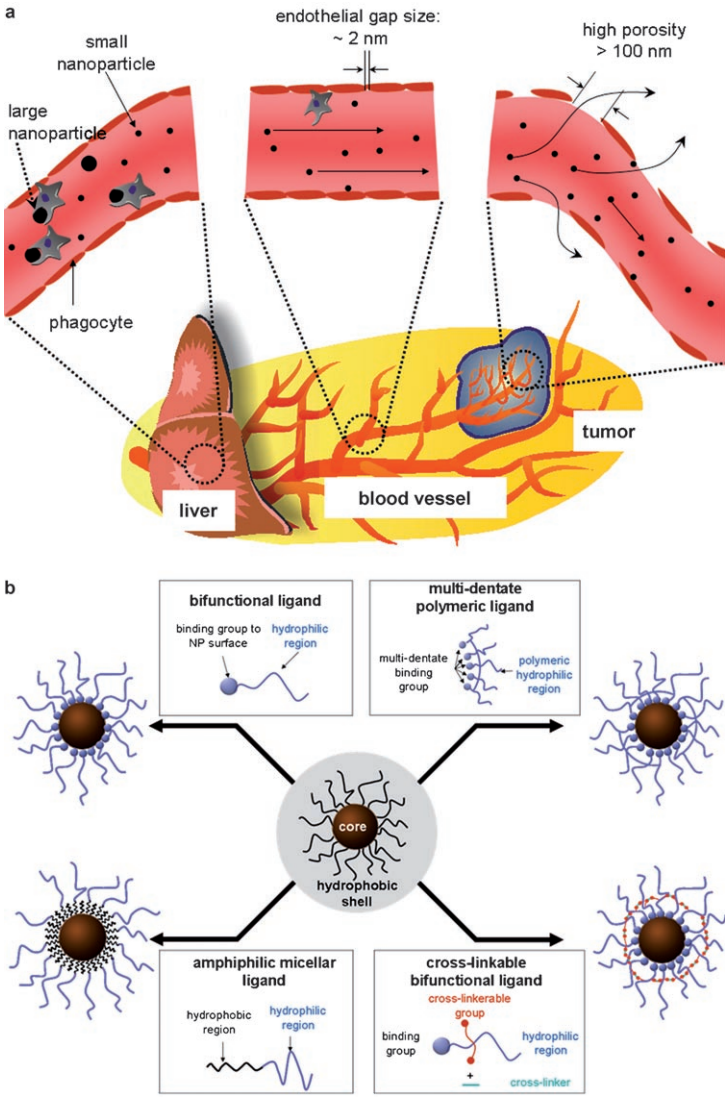

Figure 7. a) Behavior of nanoparticles in blood vessels in the liver, normal tissue, and tumor tissue regions. The enhanced permeability and retention (EPR) effect of the tailored MNPs is greatest at cancer cells. b) Surface modification strategies for designing MNP probes with high colloidal stability.

ticles allows them to form a stable colloidal dispersions in an aqueous medium (Figure 8).

2.2.2. *Multidentate Polymeric Ligands*[70–73]

The utilization of multidentate polymeric ligands also improves colloidal stability of MNPs in aqueous solutions. Surface coating γ-Fe_2O_3 nanoparticles with a PEG–polymeric phosphine oxide ligand provides them with high colloidal stability (Figure 9a,b).[70]

Inorganic polymer ligands, such as siloxane, can also be utilized. A sol–gel reaction in a microemulsion containing iron oxide nanoparticles induces formation of a silica shell around the nanoparticles (Figure 9c,d).[71,72] Reaction of triethoxysilyl-terminated PEG ligands with hydrophobically coated iron oxide nanoparticles provides them with high colloidal stability in the aqueous phase (Figure 9e,f).[73]

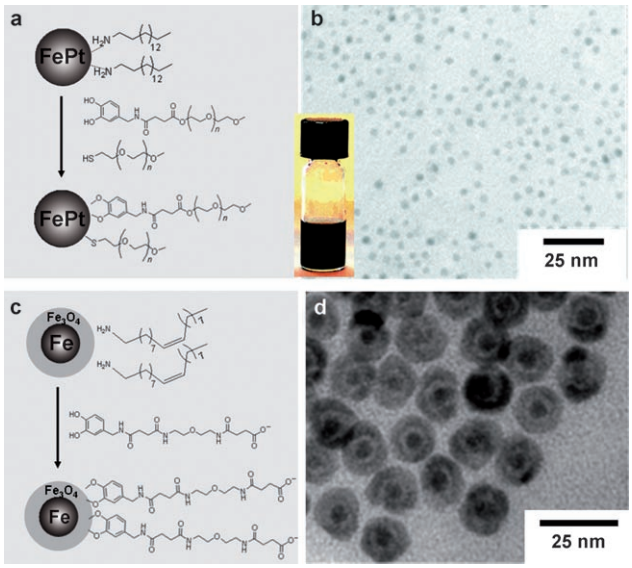

Figure 8. Nanoparticles with bifunctional ligands. a) Exchange of hydrophobic ligands on FePt nanoparticles for a mixture of polyethylene glycol PEG–dopamine and PEG–SH ligands. b) TEM image of resulting water-soluble FePt nanoparticles. Inset: aqueous solution of FePt nanoparticles. c) Exchange of ligands on Fe@Fe_3O_4 nanoparticles for PEG–dopamine. d) TEM image of water-soluble Fe@Fe_3O_4 nanoparticles (from Ref. [66, 67]).

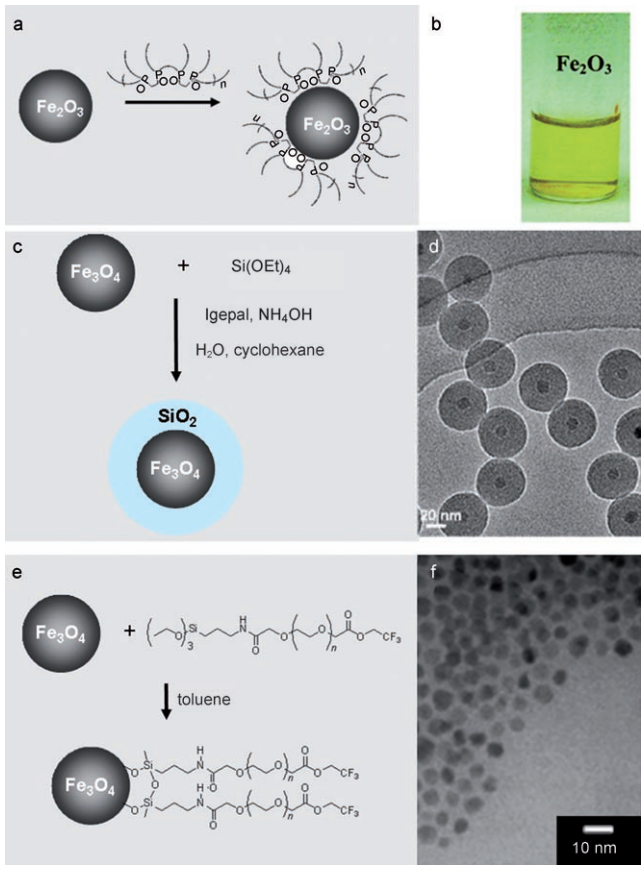

Figure 9. a, b) Synthesis scheme and demonstration of the water-solubility of multidentate polymeric ligand coated Fe_2O_3 nanoparticles (from Ref. [70]), c) synthesis scheme and d) TEM image of silicon dioxide coated Fe_3O_4 nanoparticles, e) synthesis scheme and f) TEM image of water-soluble Fe_3O_4 nanoparticles coated with PEG–siloxane ligands (from Ref. [72, 73]).

 © 2008 Wiley-VCH Verlag GmbH & Co. KGaA, Weinheim

2.2.3. Amphiphilic Micellar Coatings[74–80]

MNPs coated with hydrophobic ligands can be transferred to aqueous media by over coating them with amphiphilic ligands having both hydrophobic and hydrophilic regions. The process results in the formation of micelles. The strategy, first developed for quantum dots,[12,13] has been successfully extended to MNPs. The addition of amphiphilic ligands, such as tetradecylphosphonate and PEG-2-tetradecylether to MNPs induces the formation micelles around the MNPs[74] with the hydrophilic PEG end of the ligand contributing to the water solubility (Figure 10a,b). Similarly, water-soluble iron oxide nanoparticles are fabricated through applying a micellar coating of either amphiphilic PEG–phospholipids[75] or poly(maleic anhydride-*alt*-1-octadecene)-PEG block copolymers.[76] Encapsulation of several MNPs into each amphiphilic micelle is also possible. Owing to hydrophobic interactions, multiple MNPs are confined in the micelles formed by using the amphiphilic polystyrene–poly(acrylic acid) (PS-PAA) block copolymer (Figure 10c,d).[77] Similarly, evaporation of hydrophobic solvents containing polylactide–PEG block copolymers generate micelles of approximately 50 nm size with a hydrophobic interior containing MNPs and a hydrophilic shell (Figure 10e,f).[40]

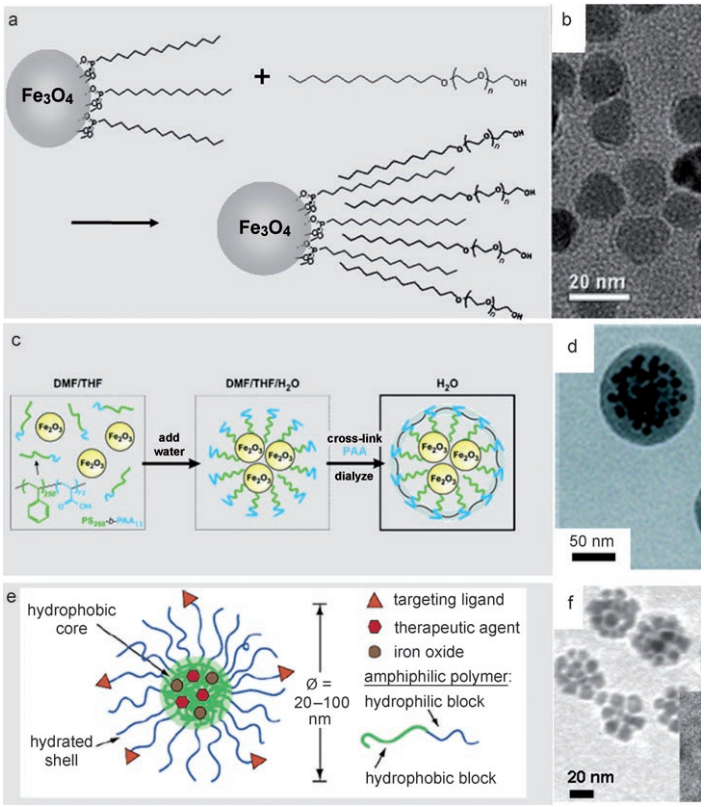

Figure 10. a) Formation of micelles around Fe_3O_4 nanoparticles with amphiphilic PEG ligands, b) TEM image of water-soluble Fe_3O_4 (from Ref. [74]), c) synthesis scheme and d) TEM image of polystyrene–poly(acrylic acid) (PS-PAA) block copolymer micelles encapsulating several MNPs. e) Schematic and f) TEM image of poly(D,L-lactide)–PEG block copolymer micelles encapsulating several MNPs and a therapeutic agent (from Ref. [40, 77]).

2.2.4. Cross-Linkable Bifunctional Ligand Coatings[37,38,41]

The use of cross-linkable small molecules as ligands can be advantageous since the cross-linking endows MNPs with high structural stability with only a marginal increase in their hydrodynamic diameter. For example, bifunctional ligand, 2,3-dimercaptosuccinic acids (DMSA), can stabilize 12 nm Fe_3O_4 nanoparticles (Figure 11a).[37,38,41] This ligand provides the nanoparticles with high colloidal stability through chelate bonding of the carboxylate group to the nanoparticles and structural stabilization by disulfide cross-linkages between the ligands. Furthermore, the remaining free thiol group of the ligand can be used for bioconjugation. These nanoparticles are fairly stable in phosphate-buffered saline (PBS, up to a NaCl concentration of 250 mM; Figure 11b), while maintaining the hydrodynamic diameter of the nanoparticles (ca. 13 nm; Figure 11c). At this size the nanoparticles are sufficiently small for in vivo utilization.

3. Molecular and Cellular MR Imaging

The designed MNPs described in the previous Sections have high MR contrast-enhancement effects as well as versatile surface ligands ready for biological conjugation. Thus, these MNPs have the potential to enable the early stage pinpointing and diagnosis of biological targets. In this Section, we will describe the effectiveness of designed MNP probes for advanced molecular and cellular imaging. Also, safety issues including cytotoxicity of MNPs will be briefly discussed.

3.1. Target-Specific Molecular Imaging

Upon conjugation with the appropriate targeting molecules, MNPs can be utilized for the active detection

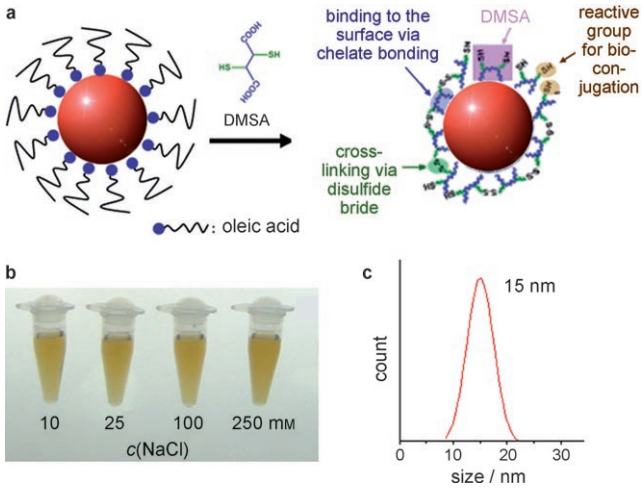

Figure 11. a) Exchange of the ligands on Fe_3O_4 nanoparticles for the cross-linkable bifunctional ligand 2,3-dimercaptosuccinic acid (DMSA), b) colloidal-stability test in NaCl solution, and c) dynamic light scattering (DLS) results of DMSA-coated Fe_3O_4 nanoparticles (from Ref. [37,41]).

 © 2008 Wiley-VCH Verlag GmbH & Co. KGaA, Weinheim

of cancer. Since less than 15% of cancer patients are diagnosed in stage I or II with conventional diagnostic tools,[81] the utilization of MNP probes with high MR contrast effects may help to improve the rate of cancer diagnosis in its earliest stages. One successful example is the molecular imaging of breast cancer using Fe_3O_4 (MEIO) nanoparticle probes. Breast cancer cells typically overexpress human epidermal growth factor receptor 2, (HER2/neu).[82] When nanoparticles with an $r2$ of 218 $mM^{-1}s^{-1}$ are conjugated with the HER2/neu specific antibody Herceptin, the SK-BR-3 breast cancer cell lines can be detected (Figure 12a).[37] Furthermore, Fe_3O_4–Herceptin probes make the ultra-sensitive in vitro detection of cancer cells possible since these probes interact with all HER2/neu positive cancer cells including Bx-PC-3 cells which have only a minimal level of HER2/neu (Figure 12b).[41]

Significantly improved molecular imaging of cancers is possible utilizing $MnFe_2O_4$ (MnMEIO) probes which have a large $r2$ of 358 $mM^{-1}s^{-1}$.[38] When these probes are intravenously injected into a mouse, very small tumors (ca. 50 mg; Figure 12c) can be detected with a high MR contrast effect (ca. 34% of $R2$ change; Figure 12d,e). When Fe_3O_4–Herceptin probes are used, a relatively weaker contrast effect with an $R2$ change of approximately 12% is observed in tumors (Figure 12d,e). However, using conventional CLIO-Herceptin probes under the same conditions, tumors will not be detected; with them there is no noticeable $R2$ change in the MR images (Figure 12d,e). Such results clearly demonstrate the significance that the magnetism-tuning of MNPs has for the ultra-sensitive imaging of cancer.

Detection of colon cancer is also possible by using Fe_3O_4–rch24 antibody conjugates.[83] With them colon cell lines with carcinoma embryogenic antigen (CEA) can be recognized, the targeted cells appearing with a dark MR contrast. Similarly, in vivo detection of colon cancer is successful (Figure 13a).

FePt–Au nanoparticles conjugated with HmenB1 antibodies, can be used to identify neuroblastoma cells (CHP-134) with a polysialic acid (PSA) overexpression. The detection is through a dark MR contrast effect in the MR image arising from the magnetic FePt component (Figure 13b).[84]

3.2. Cellular Trafficking

The migration of cells (cellular trafficking) can be monitored by MRI using MNP probes. This technique has the potential to become a powerful technique for monitoring the history and the fate of cells and for evaluating cell-based therapies. Although several SPIO-nanoparticle transfection-agent-labeling systems have been used for such purposes,[85–88] the utilization of MNP probes with defined magnetism and selected surface ligands can also be effective in cellular

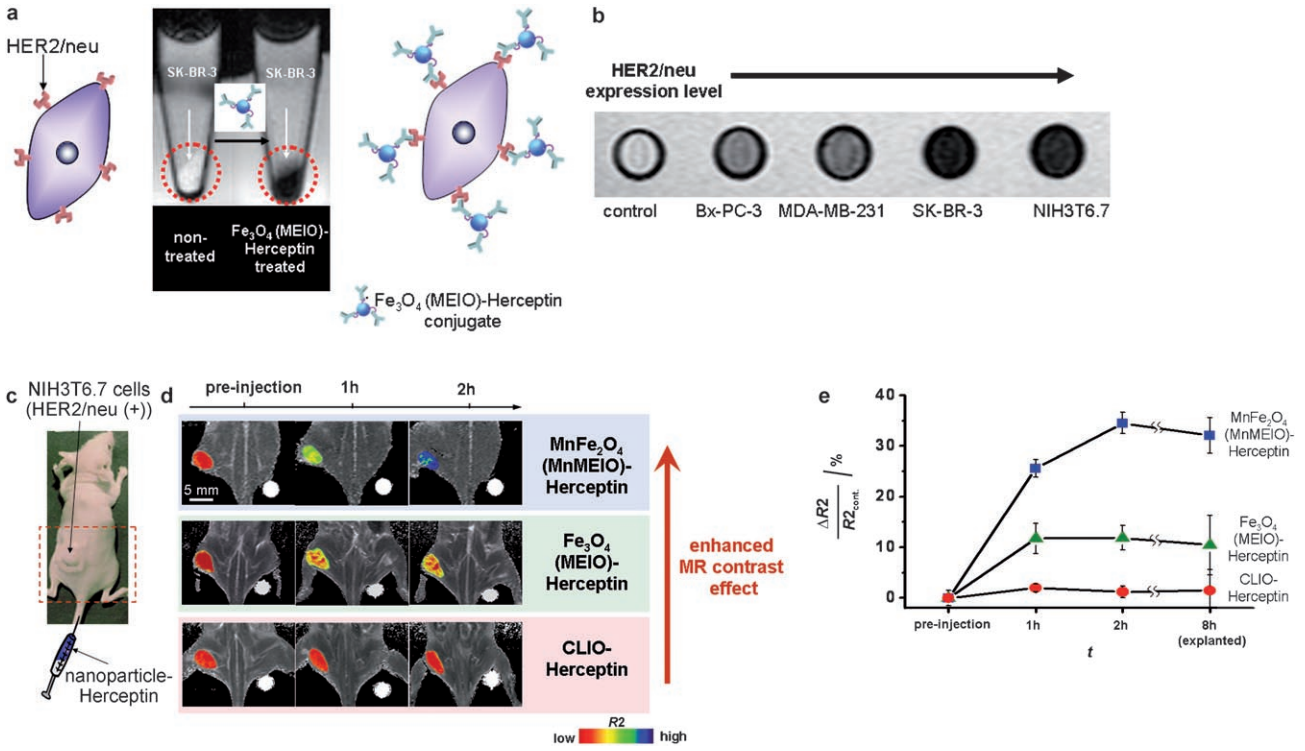

Figure 12. a) In vitro MR detection of HER2/neu-positive breast cancer (SK-BR-3) by Fe_3O_4 (MEIO)-Herceptin nanoparticle probes. b) MR contrast-enhancement effects of various cancer cells with different HER2/neu expression levels (from Ref. [37, 41]), c–e) Highly-sensitive in vivo cancer detection by utilization of $MnFe_2O_4$ (MnMEIO)-Herceptin nanoparticle probes. c) Intravenous tail-vein injection of the MEIO-Herceptin probes into a mouse with a small (ca. 50 mg) HER2/neu positive cancer in its proximal femur region. For comparison, MEIO-Herceptin probes and CLIO-Herceptin probes were also tested. d) Color-mapped MR images of the mouse at different times following injection. e) Time-dependent $R2$ changes at the tumor site after injection of the probes (from Ref. [38]).

 © 2008 Wiley-VCH Verlag GmbH & Co. KGaA, Weinheim

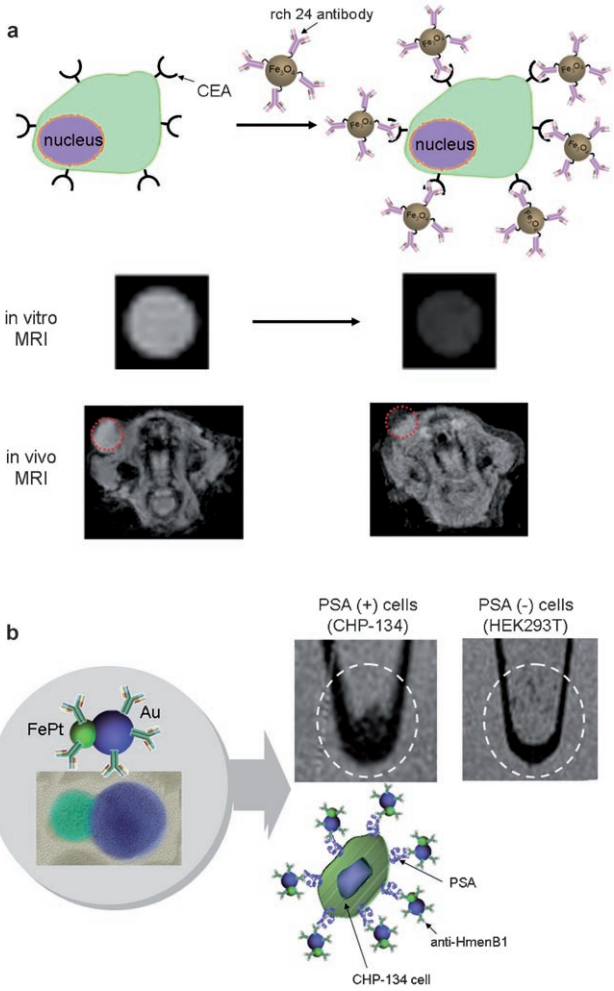

Figure 13. a) MR detection of carcinoma embryogenic antigen (CEA) positive colon cancer by Fe_3O_4-rch 24 antibody conjugates: schematic representation of molecular recognition by the nanoparticle probes and the in vitro and in vivo MR detection of colon cancer (from Ref. [83]), b) MR detection of neuroblastoma cancer cell (CHP-134) using dumbbell shaped FePt-Au and HmenB1 antibody conjugates (from Ref. [84]).

trafficking MRI studies. For example, the use of a new type of FeCo metal alloy MNP probes with high MR contrast effects ($r2 = 644\ mM^{-1}s^{-1}$) can provide excellent cellular MR signals.[39] When these nanoparticles are co-cultivated with mesenchymal stem cells (MSCs), the nanoparticle-labeled MSCs show an enhanced MR contrast compared to Feridex-labeled cells (Figure 14).

Fe_3O_4 MNPs coated with appropriate surface ligands can be effectively transported inside cells. By using (3-carboxypropyl)trimethylammonium chloride molecules, cationic-ligand-coated MNPs can be prepared which show a much higher transfection efficiency into neural stem cells (NSCs) than both anionic ligand (2-carboxyethyl phosphonate) coated MNPs and conventional Poly-L-lysine-Feridex (Figure 15a).[42] This improved cellular transfection capability allows for the in vivo cellular MRI of NSC trafficking, in which the longitudinal migration of NSCs is clearly observed in MR images as an elongated dark region along the spinal cord (Figure 15b).

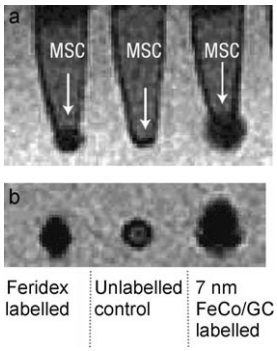

Figure 14. MR images of Feridex-labeled, unlabeled, and FeCo metal-alloy MNP labeled mesenchymal stem (MSC) cells, a) oblique plane, b) coronal plane (from Ref. [39]).

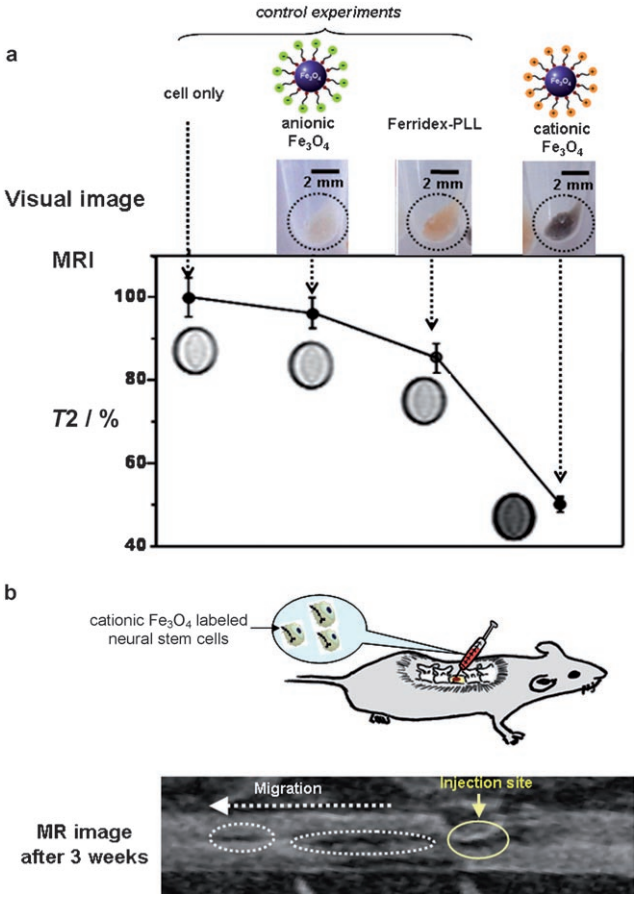

Figure 15. a) Effects of the surface ligands of Fe_3O_4 nanoparticles on cellular labeling and MR contrast enhancement. Cationic Fe_3O_4 nanoparticles show the most pronounced MR contrast effects, Ferridex-PLL is used in conventional cell labeling. b) In vivo trafficking of cationic Fe_3O_4 labeled neural stem cells (NSCs) introduced into the spinal cord of a mouse (from Ref. [42]).

3.3. Biosafety of MNPs

The toxicity of MNPs is also a very important issue that needs to be addressed prior to clinical utilization. According to previous toxicity studies on iron oxide nanoparticles, they appear to be biologically safe.[22,89,90] They are metabolized

 © 2008 Wiley-VCH Verlag GmbH & Co. KGaA, Weinheim

into elemental iron species by either hydrolytic enzymes or the acidic conditions found inside lysosomes. Although high concentrations of Fe ions in cytoplasm can potentially cause the generation of reactive oxygen species (ROS), ferritin and transferrin receptors regulate the homeostasis of iron.[91] The iron is then merged in normal body stores and are subsequently incorporated in hemoglobin. The novel iron oxide MNPs show the low toxicity typical of the conventional iron oxide nanoparticles. No noticeable cytotoxic effect is observed when Fe_3O_4 and $MnFe_2O_4$ nanoparticles are tested to various cell lines up to the highest tested concentration of 200 $\mu g\,mL^{-1}$.[38]

Metal-alloy MNPs, such as FeCo and FePt, can potentially cause some toxicity owing to the highly reactive natures of Co and Pt ions. This toxicity can be avoided by using appropriate coatings. For example, thick graphite shell coatings on FeCo nanoparticles prevent metal ions leaching from them.[39] When they are tested both in vitro in cells and in vivo in rabbits, no acute toxicity is observed. Despite these promising results, further systematic safety evaluations of these new types of engineered MNPs with respect to bio-distribution, body clearance, and long term toxicity are required.[92,93]

4. Hybrid MNPs as Multimodal Molecular Imaging Probes

The multimodality of hybrid nanoparticles suggests the possibility of multiple imaging techniques (e.g. magnetic and optical) or combining different multiple functionalities (e.g. imaging and therapeutics). One such example is a probe in which MNPs are coupled with other functional nanoparticles (e.g. probing or therapeutic) so as to serve as a multimodal probe for biomedical applications. For this purpose, hybrid "core–satellite" nanoparticles composed of a dye-doped silica "core" (Dye-SiO_2) and multiple "satellites" of Fe_3O_4 nanoparticles have been reported.[94] They exhibit a 3.4 times larger MR contrast effect than in the individual nanoparticles. This increase arises from cooperative magnetic interactions between the linked MNPs (Figure 16a). By conjugating nanoparticles with the HmenB1 antibody which specifically binds to the polysialic acid (PSA), the resulting conjugates can be used to detect PSA positive cells (CHP-134), these show up with a dark MR contrast (Figure 16b). In addition, a strong red fluorescence is observed from the membrane regions of the CHP-134 cells (Figure 16c).[95] This result suggests that dual-mode imaging is clearly advantageous in obtaining both macroscopic (e.g. MRI) and microscopic subcellular (e.g. optical imaging) information of biological events.

Hybrid metal-alloy MNPs can have therapeutic capabilities in addition to MR imaging capabilities. For example, when HeLa cells are treated with FePt@CoS_2 nanoparticles, cell viability is dramatically decreased.[96] After cellular uptake of FePt@CoS_2 nanoparticles the low pH value (ca. 5.5) of the cellular environment induces oxidation of Pt and the subsequent release of Pt^{2+} ions, which causes DNA damage and cell apoptosis. The cytotoxic effect of FePt@CoS_2 can be confirmed by changes in cell morphologies and dose-dependent cell viability (Figure 17a).

Hybrid nanoparticles of SiO_2@Fe_3O_4@Au can be used for molecular MR imaging and cancer therapy (Figure 17b).[97] After conjugation with an anti-HER2/neu antibody and subsequent treatment to breast cancer cells, a dark MR contrast is observed for the cells in the *T*2-weighted MRI, indicating successful HER2/neu targeting. Upon irradiation by a continuous-wave (CW) laser, the targeted cells are killed by hyperthermia effects arising from the Au shells.

Encapsulation of the therapeutic agents and MNPs inside polymeric micelles is also effective for simultaneous diagnosis and therapy. Polymeric micelle nanoparticles containing MNPs, doxorubicin and the tripeptide Arg-Gly-Asp (RGD), which is a targeting moiety for angiogenesis-related $\alpha_v\beta_3$ integrin, have been prepared. When endothelial cells are treated with these micelles, they could be detected by MRI and therapeutic effects on the targeted cells were clearly observed (Figure 17c).[40]

5. Concluding Remarks

Designed MNPs with controllable nanoscale properties, such as size, composition, magnetism, and surface states are valuable not only for high MR contrast enhancement but also for excellent colloidal-stability and targeting capabilities. Although the development of designed MNP probes is still

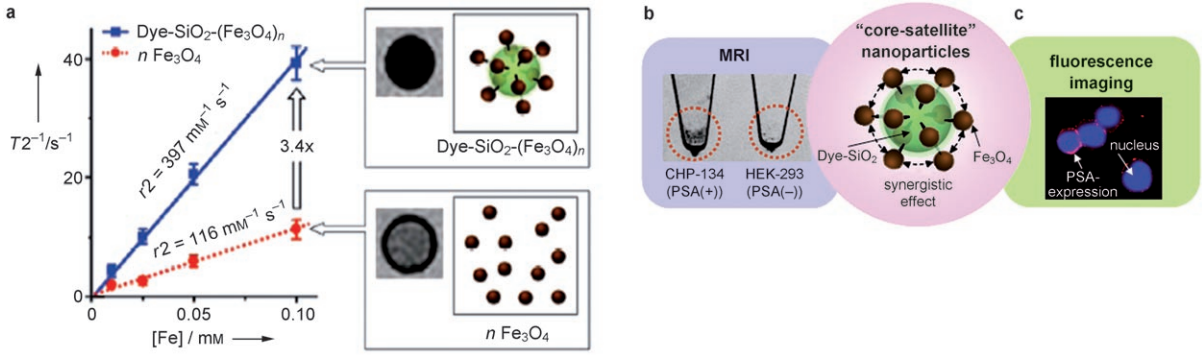

Figure 16. Hybrid Fe_3O_4 and dye-doped silica (Dye-SiO_2) nanoparticles for dual mode MR–fluorescent imaging of neuroblastoma. a) Increased MR contrast enhancement by Dye-SiO_2–$(Fe_3O_4)_n$ core–satellite NPs and their dual-modal imaging applications in detection of polysialic acid (PSA) expressed in neuroblastoma b) MRI (PSA-negative HEK 293 cells (right) are not visible.) and c) fluorescence (from Ref. [94]).

 © 2008 Wiley-VCH Verlag GmbH & Co. KGaA, Weinheim

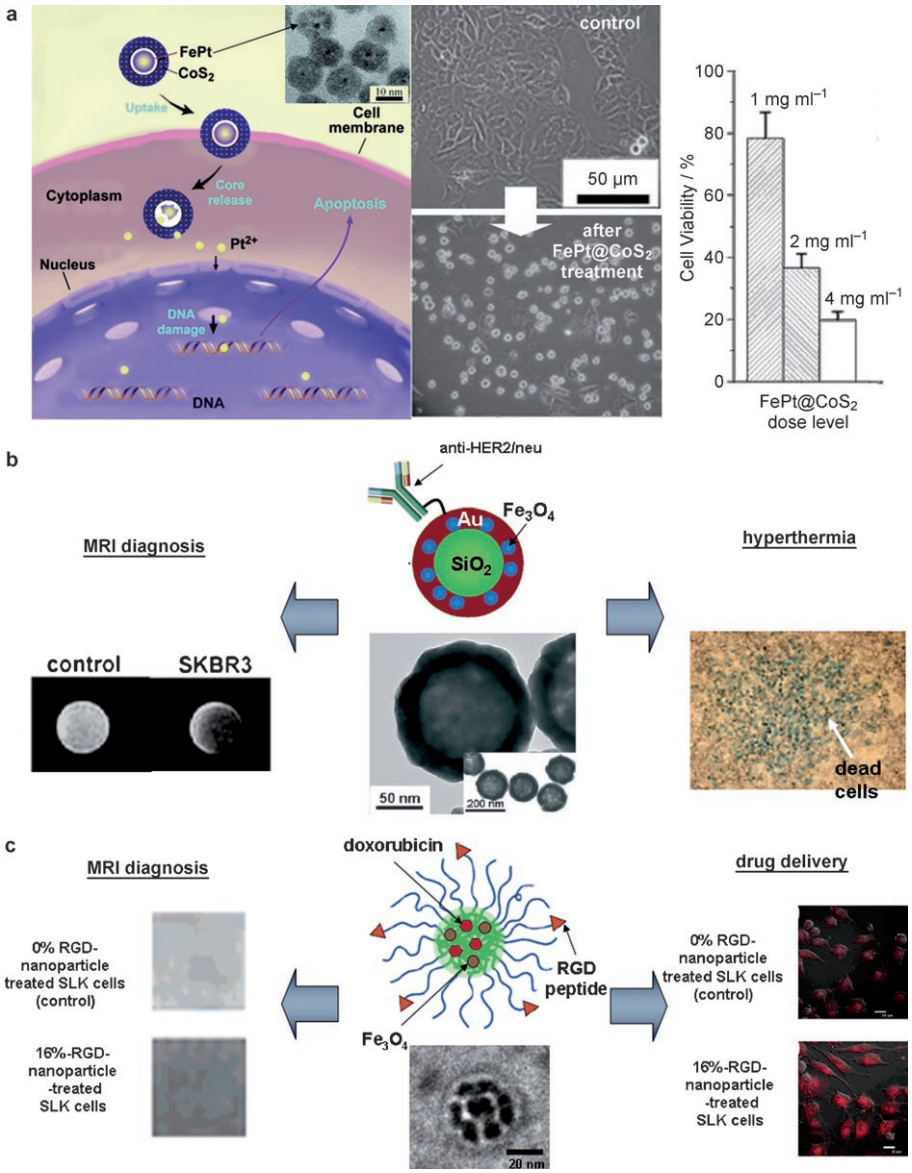

Figure 17. a) Therapeutic applications of hybrid FePt@CoS_2 metal-alloy MNPs. Left: the lethal effect of the hybrid MNPs on cells. Middle: optical detection of changes in cell morphology of untreated HeLa cells (top) and the MNP-treated HeLa cells (bottom). Right: dose-dependent cell viability (from Ref. [96]), b) hybrid iron oxide nanoparticles consisting of SiO_2@Fe_3O_4@Au and anti-HER2/neu-antibody for simultaneous MRI diagnosis and laser-assisted hyperthermia therapy (from Ref. [97]), c) Micelle-based hybrid nanoparticles containing iron oxide nanoparticles, doxorubicine, and RGD peptides for the MR detection and therapy of angiogenic cells with overexpression of $\alpha_v\beta_3$ integrin. Fluorescence images of cells with micelles that contain 0% RGD peptide (control) and 16% RGD peptide indicate effective drug delivery (from Ref. [40]). RGD = tripeptide Arg-Gly-Asp.

in its early stages, they have the potential to bring significant advances to the biomedical imaging fields. For example, tailored MNP probes could pave the way to in vivo diagnosis of the early stages of many diseases and shed light on biological processes such as cancer development and metastasis, cell evolution, and cell-to-cell interactions.

We thank Mi-yun Kim for her kind help in the preparation of the manuscript. This research is supported by the National Research Laboratory (M10600000255), NCRC (Grant R15-2004-024-02002-0), and NCI Center for Cancer Nanotechnoloogy Excellence (CCNE), Nano/Bio Science & Technology Program (M10503000218-05M0300-21810), AFOSR (FA4869-07-1-4016), the Korea Research Council of Fundamental Science and Technology, and 2nd stage BK21 for Chemistry.

Received: April 16, 2007

[1] T. F. Massoud, S. S. Gambhir, *Gene. Dev.* **2003**, *17*, 545–580.
[2] K. Shah, A. Jacobs, X. O. Breakefield, R. Weissleder, *Gene Ther.* **2004**, *11*, 1175–1187.
[3] D. G. Mitchell, *MRI Principles*, W. B. Saunders Company, Philadelphia, **1999**.
[4] A. P. Alivisatos, *Nat. Biotechnol.* **2004**, *22*, 47–52.
[5] X. Michalet, F. F. Pinaud, L. A. Bentolila, J. M. Tsay, S. Doose, J. J. Li, G. Sundaresan, A. M. Wu, S. S. Gambhir, S. Weiss, *Science* **2005**, *307*, 538–544.
[6] I. L. Medintz, H. T. Uyeda, E. R. Goldman, H. Mattoussi, *Nat. Mater.* **2005**, *4*, 435–446.
[7] R. Weissleder, A. S. Lee, A. J. Fischman, P. Reimer, T. Shen, R. Wilkinson, R. J. Callahan, T. J. Brady, *Radiology* **1991**, *181*, 245–249.
[8] J. W. M. Bulte, D. L. Kraitchman, *NMR Biomed.* **2004**, *17*, 484–499.
[9] C. A. Mirkin, C. M. Niemeyer, *Nanobiotechnology II: More Concepts and Applications*, Wiley-VCH, Weinheim, **2007**.
[10] W. Li, F. C. Szoka, Jr., *Pharm. Res.* **2007**, *24*, 438–449.
[11] M. C. Garnett, P. Kallinteri, *Occup. Med.* **2006**, *56*, 307–311.
[12] X. Wu, H. Liu, J. Liu, K. N. Haley, J. A. Treadway, J. P. Larson, N. Ge, F. Peale, M. P. Bruchez, *Nat. Biotechnol.* **2003**, *21*, 41–46.
[13] X. Gao, Y. Cui, R. M. Levenson, L. W. K. Chung, S. Nie, *Nat. Biotechnol.* **2004**, *22*, 969–976.
[14] L. He, M. D. Musick, S. R. Nicewarner, F. G. Salinas, S. J. Benkovic, M. J. Natan, C. D. Keating, *J. Am. Chem. Soc.* **2000**, *122*, 9071–9077.
[15] Y. W. C. Cao, R. C. Jin, C. A. Mirkin, *Science* **2002**, *297*, 1536–1540.
[16] R. Elghanian, J. J. Storhoff, R. C. Mucic, R. L. Letsinger, C. A. Mirkin, *Science* **1997**, *277*, 1078–1081.
[17] C. Sönnichsen, B. M. Reinhard, J. Liphardt, A. P. Alivisatos, *Nat. Biotechnol.* **2005**, *23*, 741–745.
[18] M. Y. Han, X. H. Gao, J. Z. Su, S. Nie, *Nat. Biotechnol.* **2001**, *19*, 631–635.
[19] A. A. Chen, A. A. Derfus, S. R. Khetani, S. N. Bhatia, *Nucleic Acids Res.* **2005**, *33*, e190.

 © 2008 Wiley-VCH Verlag GmbH & Co. KGaA, Weinheim

[20] Z. Medarova, W. Pham, C. Farrar, V. Petkova, A. Moore, *Nat. Med.* **2007**, *13*, 372 – 377.
[21] R. Weissleder, A. Moore, U. Mahmood, R. Bhorade, H. Benveniste, E. A. Chiocca, J. P. Basilion, *Nat. Med.* **2000**, *6*, 351 – 354.
[22] Y.-X. J. Wang, S. M. Hussain, G. P. Krestin, *Eur. Radiol.* **2001**, *11*, 2319 – 2331.
[23] M. F. Bellin, *Eur. J. Radiol.* **2006**, *60*, 314 – 323.
[24] M. Zhao, D. A. Beauregard, L. Loizou, B. Davletov, K. M. Brindle, *Nat. Med.* **2001**, *7*, 1241 – 1244.
[25] J. Rockenberger, E. C. Sher, A. P. Alivisatos, *J. Am. Chem. Soc.* **1999**, *121*, 11595 – 11596.
[26] S. H. Sun, H. Zeng, D. B. Robinson, S. Raoux, P. M. Rice, S. X. Wang, G. X. Li, *J. Am. Chem. Soc.* **2004**, *126*, 273 – 279.
[27] T. Hyeon, *Chem. Commun.* **2003**, 927 – 934.
[28] J. Park, K. An, Y. Hwang, J.-G. Park, H.-J. Noh, J.-Y. Kim, J.-H. Park, N.-M. Hwang, T. Hyeon, *Nat. Mater.* **2004**, *3*, 891 – 895.
[29] N. R. Jana, Y. Chen, X. Peng, *Chem. Mater.* **2004**, *16*, 3931 – 3935.
[30] Y. Jun, J. Choi, J. Cheon, *Chem. Commun.* **2007**, 1203 – 1214.
[31] J. Cheon, N.-J. Kang, S.-M. Lee, J.-H. Yoon, S. J. Oh, *J. Am. Chem. Soc.* **2004**, *126*, 1950 – 1951.
[32] A.-H. Lu, E. L. Salabas, F. Schüth, *Angew. Chem.* **2007**, *119*, 1242 – 1266; *Angew. Chem. Int. Ed.* **2007**, *46*, 1222 – 1244.
[33] E. V. Shevchenko, D. V. Talapin, A. L. Rogach, A. Kornowski, M. Haase, H. Weller, *J. Am. Chem. Soc.* **2002**, *124*, 11480 – 11485.
[34] J. B. Tracy, D. N. Weiss, D. P. Dinega, M. G. Bawendi, *Phys. Rev. B* **2005**, *72*, 064404.
[35] S. Sun, *Adv. Mater.* **2006**, *18*, 393 – 403.
[36] V. F. Puntes, K. M. Krishnan, A. P. Alivisatos, *Science* **2001**, *291*, 2115 – 2117.
[37] Y. Jun, Y.-M. Huh, J.-s. Choi, J.-H. Lee, H.-T. Song, S. J. Kim, S. Yoon, K.-S. Kim, J.-S. Shin, J.-S. Suh, J. Cheon, *J. Am. Chem. Soc.* **2005**, *127*, 5732 – 5733.
[38] J.-H. Lee, Y.-M. Huh, Y.-w. Jun, J.-w. Seo, J.-t. Jang, H.-T. Song, S. Kim, E.-J. Cho, H.-G. Yoon, J.-S. Suh, J. Cheon, *Nat. Med.* **2007**, *13*, 95 – 99.
[39] W. S. Seo, J. H. Lee, X. Sun, Y. Suzuki, D. Mann, Z. Liu, M. Terashima, P. C. Yang, M. V. McConnell, D. G. Nishimura, H. Dai, *Nat. Mater.* **2006**, *5*, 971 – 976.
[40] N. Nasongkla, E. Bey, J. Ren, H. Ai, C. Khemtong, J. S. Guthi, S.-F. Chin, A. D. Sherry, D. A. Boothman, J. Gao, *Nano Lett.* **2006**, *6*, 2427 – 2430.
[41] Y.-M. Huh, Y. Jun, H.-T. Song, S. J. Kim, J.-s. Choi, J.-H. Lee, S. Yoon, K.-S. Kim, J.-S. Shin, J.-S. Suh, J. Cheon, *J. Am. Chem. Soc.* **2005**, *127*, 12387 – 12391.
[42] H.-T. Song, J.-s. Choi, Y.-M. Huh, S. Kim, Y.-w. Jun, J.-S. Suh, J. Cheon, *J. Am. Chem. Soc.* **2005**, *127*, 9992 – 9993.
[43] S. H. Koenig, K. E. Keller, *Magn. Reson. Med.* **1995**, *34*, 227 – 233.
[44] J. Park, J. Joo, S. G. Kwon, Y. Jang, T. Hyeon, *Angew. Chem.* **2007**, *119*, 4714 – 4745; *Angew. Chem. Int. Ed.* **2007**, *46*, 4630 – 4660.
[45] C. B. Murray, C. R. Kagan, M. G. Bawendi, *Annu. Rev. Mater. Sci.* **2000**, *30*, 545 – 610.
[46] T. Vossmeyer, L. Katsikas, M. Giersig, I. G. Popovic, K. Diesner, A. Chemseddine, A. Eychmüller, H. Weller, *J. Phys. Chem.* **1994**, *98*, 7665 – 7673.
[47] Y. Jun. J.-H. Lee, J.-s. Choi, J. Cheon, *J. Phys. Chem. B* **2005**, *109*, 14795 – 14806.
[48] Y. Jun, J.-s. Choi, J. Cheon, *Angew. Chem.* **2006**, *118*, 3492 – 3517; *Angew. Chem. Int. Ed.* **2006**, *45*, 3414 – 3439.
[49] M. P. Morales, S. Veintemillas-Verdaguer, M. I. Montero, C. J. Serna, *Chem. Mater.* **1999**, *11*, 3058 – 3064.
[50] R. A. McCurrie, *Ferromagnetic Materials: Structure and Properties*, Academic Press, San Diego, **1994**.
[51] R. Weissleder, D. D. Stark, B. L. Engelastad, B. R. Bacon, C. C. Compton, D. L. White, P. Jacobs, J. Lewis, *Am. J. Roentgenol.* **1989**, *152*, 167 – 173.
[52] P. Reimer, E. J. Rummeny, H. E. Daldrup, T. Balzer, B. Tombach, T. Berns, P. E. Peters, *Radiology* **1995**, *195*, 489 – 496.
[53] C. W. Jung, P. Jacobs, *Magn. Reson. Imaging* **1995**, *13*, 661 – 674.
[54] L. Josephson, C.-H. Tung, A. Moore, R. Weissleder, *Bioconjugate Chem.* **1999**, *10*, 186 – 191.
[55] J.-I. Park, J. Cheon, *J. Am. Chem. Soc.* **2001**, *123*, 5743 – 5746.
[56] B. D. Cullity, *Introduction to Magnetic Materials*, Addison-Wesley Publishing, Philippinen, **1972**.
[57] S. Trattnig, K. Pinker, A. Ba-Saalamah, I. M. Nobauer-Huhmann, *Eur. Radiol.* **2006**, *16*, 1280 – 1287.
[58] G. J. Strijkers, W. J. Mulder, G. A. Van Tilborg, K. Nicolay, *Anti-Cancer Agents Med. Chem.* **2007**, *7*, 291 – 305.
[59] A. Tanimoto, S. Kuribayashi, *Eur. J. Radiol.* **2006**, *58*, 200 – 216.
[60] A. K. Gupta, S. Wells, *IEEE Trans. Nanobiosci.* **2004**, *3*, 66 – 73.
[61] J. A. Firth, *J. Anat.* **2002**, *200*, 541 – 548.
[62] A. Hirano, T. Matsui, *Hum. Pathol.* **1975**, *6*, 611 – 621.
[63] Q. Liu, Z. Xu, *Langmuir* **1995**, *11*, 4617 – 4622.
[64] A. B. Bourlinos, A. Bakandritos, V. Georgakilas, D. Petridis, *Chem. Mater.* **2002**, *14*, 3226 – 3228.
[65] V. Salgueirino-Maceira, L. M. Liz-Marzan, M. Farle, *Langmuir* **2004**, *20*, 6946 – 6950.
[66] R. Hong, N. O. Fischer, T. Emrick, V. M. Rotello, *Chem. Mater.* **2005**, *17*, 4617 – 4621.
[67] S. Peng, C. Wang, J. Xie, S. Sun, *J. Am. Chem. Soc.* **2006**, *128*, 10676 – 10677.
[68] A. H. Latham, M. E. Williams, *Langmuir* **2006**, *22*, 4319 – 4326.
[69] J. Xie, C. Xu, Z. Xu, Y. Hou, K. L. Young, S. X. Wang, N. Pourmand, S. Sun, *Chem. Mater.* **2006**, *18*, 5401 – 5403.
[70] S.-W. Kim, S. Kim, J. B. Tracy, A. Jasanoff, M. G. Bawendi, *J. Am. Chem. Soc.* **2005**, *127*, 4556 – 4557.
[71] D. K. Yi, S. T. Selvan, S. S. Lee, G. C. Papaefthymiou, D. Kundaliya, J. Y. Ying, *J. Am. Chem. Soc.* **2005**, *127*, 4990 – 4991.
[72] D. K. Yi, S. S. Lee, G. C. Papaefthymiou, J. Y. Ying, *Chem. Mater.* **2006**, *18*, 614 – 619.
[73] N. Kohler, G. E. Fryxell, M. Zhang, *J. Am. Chem. Soc.* **2004**, *126*, 7206 – 7211.
[74] D. B. Robinson, H. H. J. Persson, H. Zeng, G. Li, N. Pourmand, S. Sun, S. X. Wang, *Langmuir* **2005**, *21*, 3096 – 3103.
[75] N. Nitin, L. E. LaConte, O. Zurkiya, X. Hu, G. Bao, *J. Biol. Inorg. Chem.* **2004**, *9*, 706 – 712.
[76] W. W. Yu, E. Chang, C. M. Sayes, R. Drezek, V. L. Colvin, *Nanotechnology* **2006**, *17*, 4483 – 4487.
[77] B.-S. Kim, J.-M. Qiu, J.-P. Wang, T. A. Taton, *Nano Lett.* **2005**, *5*, 1987 – 1991.
[78] B. Ceyhan, P. Alhorn, C. Lang, D. Schuler, C. M. Niemeyer, *Small* **2006**, *2*, 1251 – 1255.
[79] S. G. Grancharov, H. Zeng, S. Sun, S. X. Wang, S. O'Brien, C. B. Murray, J. R. Kirtley, G. A. Held, *J. Phys. Chem. B* **2005**, *109*, 13030 – 13035.
[80] R. DePalma, S. Peeters, M. J. van Bael, H. V. den Rul, K. Bonroy, W. Laureyn, J. Mullens, G. Borghs, G. Maes, *Chem. Mater.* **2007**, *19*, 1821 – 1831.
[81] American Cancer Society, *Cancer Facts*, American Cancer Society, Atlanta, **2005**.
[82] D. Vernimmen, M. Gueders, S. Pisvin, P. Delvenne, R. Winkler, *Br. J. Cancer* **2003**, *89*, 899 – 906.
[83] F. Hu, L. Wei, Z. Zhou, Y. Ran, Z. Li, M. Gao, *Adv. Mater.* **2006**, *18*, 2553 – 2556.
[84] J.-s. Choi, Y.-w. Jun, S.-I. Yeon, H. C. Kim, J.-S. Shin, J. Cheon, *J. Am. Chem. Soc.* **2006**, *128*, 15982 – 15983.
[85] S. Miyoshi, J. A. Flexman, D. J. Cross, K. R. Maravilla, Y. Kim, Y. Anzai, J. Oshima, S. Minoshima, *Mol. Imaging Biol.* **2006**, *7*, 286 – 195.

 © 2008 Wiley-VCH Verlag GmbH & Co. KGaA, Weinheim

[86] P. Smirnov, E. Lavergne, F. Gazeau, M. Lewin, A. Boissonnas, B. T. Doan, B. Gillet, C. Combadiere, B. Combadiere, O. Clement, *Magn. Reson. Med.* **2006**, *56*, 498 – 508.
[87] J. A. Frank, B. R. Miller, A. S. Arbab, H. A. Zywicke, E. K. Jordan, B. K. Lewis, L. H. Bryant Jr. , J. W. Bulte, *Radiology* **2003**, *228*, 480 – 487.
[88] A. S. Arbab, G. T. Yocum, L. B. Wilson, A. Parwana, E. K. Jordan, H. Kalish, J. A. Frank, *Mol. Imaging* **2004**, *3*, 24 – 32.
[89] C. Kumar, *Nanomaterials for Cancer Diagnosis*, Wiley-VCH, Weinheim, **2007**.
[90] R. Lawrence, *PDA J. Pharm. Sci. Technol.* **1998**, *52*, 190 – 198.
[91] E. C. Theil, *J. Nutr.* **2003**, *133*, 1649S – 1655S.
[92] A. Nel, *Science* **2005**, *308*, 804 – 806.
[93] A. D. Maynard, *Nanotoday* **2006**, *1*, 22 – 33.
[94] J.-H. Lee, Y.-w. Jun, S.-I. Yeon, J.-S. Shin, J. Cheon, *Angew. Chem.* **2006**, *118*, 8340 – 8342; *Angew. Chem. Int. Ed.* **2006**, *45*, 8160 – 8162.
[95] U. Rutishauser, M. Watanabe, J. Silver, F. A. Troy, E. R. Vimr, *J. Cell Biol.* **1985**, *101*, 1842 – 1849.
[96] J. Gao, G. Liang, B. Zhang, Y. Kuang, X. Zhang, B. Xu, *J. Am. Chem. Soc.* **2007**, *129*, 1428 – 1433.
[97] J. Kim, J. E. Lee, J. Lee, Y. Jang, S. W. Kim, K. An, J. H. Yu, T. Hyeon, *Angew. Chem.* **2006**, *118*, 4907 – 4911; *Angew. Chem. Int. Ed.* **2006**, *45*, 4789 – 4793.

 © 2008 Wiley-VCH Verlag GmbH & Co. KGaA, Weinheim